scientific reports

Check for updates

OPEN

# A low-profile 3-D printable metastructure for performance improvement of aperture antennas

Md Yeakub Ali[1]✉, Ali Lalbakhsh[1]✉, Slawomir Koziel[2,3], Lukasz Golunski[3], Foez Ahmed[4] & Mohsen Asadnia[1]

**In order to increase the radiation performance of aperture-type antennas, this paper demonstrates a low-profile, planar, single-layer, three-dimensional (3-D) printable metastructure. The proposed hybridized metastructure is highly transparent as it is made out of novel hybrid meta-atoms having transmission coefficient magnitudes greater than – 0.72 dB and fully complies with the near-field phase transformation principle. The hybridized design approach makes the metastructure planar, low-profile, light in weight, and compatible with additive printing technology. For the proof-of-concept, such metastructure is developed and numerically verified to enhance the radiation performance of a resonant cavity antenna (RCA). With the proposed metastructure, the peak directivity of the RCA is improved by 8.6 dBi (from 11.4 dBi to 20 dBi) at the operating frequency of 12.4 GHz. The aperture efficiency and 3-dB directivity bandwidth of the RCA with the metastructure are 41.46% and 16.5%, respectively. Using readily accessible thermoplastics or polymers and copper with cost-effective fused deposition modeling (FDM) 3-D printing technology, the proposed planar hybridized metastructure can be prototyped commercially.**

Additive manufacturing (AM), also widely known as three-dimensional (3-D) printing technology, has been a pivotal part of the sustainable Fourth Industrial Revolution[1]. This environment-friendly technology is continuously expanding the potential of new business markets throughout the world and is projected to create a market worth 130 billion euros in the upcoming decade[2]. Currently, this technology is widely adopted across different sectors, especially in the automotive industry[3], aerospace[4], defense[5], healthcare[6], and microwave communication, due to its numerous excellent characteristics. 3-D printing enables rapid prototyping, precise fabrication, and error detection and correction before production. It also enables efficiency in mass production with the help of artificial intelligence and IoT. Modern 3-D printers are capable of fabricating highly complex structures using multi-materials, which is very challenging in conventional subtractive manufacturing methods. Miniaturized structures are particularly difficult to produce using conventional subtractive manufacturing techniques like drilling, milling, and reaming[7]. In contrast, 3-D printers can fabricate the whole structure in a single step, resulting in more robust structures, whereas conventional manufacturing requires human intervention to integrate multiple parts. Additionally, due to automatic machine printing and low-cost 3-D printing materials, 3-D printing is more cost-effective than conventional manufacturing methods[8].

Highly directive antennas are desirable for applications such as satellite communication, radar, and wireless backhaul networks for effective long-distance and interference-free communication[9,10]. Conventional parabolic dish[11] and horn antennas are not practical in some modern applications due to their bulky and heavy design. While antenna arrays[12,13] offer high gain and superior performance, they are costly due to the complexity of their phase-shifting networks. Reflectarray[14–17] and transmitarray[18–20] antennas are used in some applications as a high-gain solution, but they require a feed horn to be placed at a focal distance from the reflect or transmit array structure, which increases the overall antenna profile. Resonant cavity antennas[21,22], also known as Fabry-Perot (FP) resonator antennas or EBG resonator antennas[23,24], are considered an excellent alternative to medium-to-high gain applications in some state-of-the-art technologies. Their planar surface, simple feeding system, and easy fabrication process make them highly advantageous[25].

[1]School of Engineering, Macquarie University, Sydney, NSW 2109, Australia. [2]Engineering Optimization & Modeling Center, Department of Engineering, Reykjavik University, Reykjavik, Iceland. [3]Faculty of Electronics, Telecommunications and Informatics, Department of Microelectronics Systems, Gdansk University of Technology, Gdansk, Poland. [4]Department of Information and Communication Engineering, University of Rajshahi, Rajshahi, Bangladesh. ✉email: mdyeakub.ali@students.mq.edu.au; ali.lalbakhsh@mq.edu.au

The near-field phase transformation (NFPT) approach can be applied to develop low-profile phase-correcting metastructures (PCMs) that enhance the far-field radiation performance of aperture-type antennas[26]. One successful attempt for near-field phase correction was reported in Ref.[23] for performance enhancement of aperture-type antenna by applying the principle of the Risley prism[27]. In this approach, the proposed PCM, designed by applying the NFPT technique, is placed on top of the base antenna aperture at a specific distance to transform the typically non-uniform phases of the aperture antennas into a more uniform distribution, thereby improving the far-field radiation performance. Depending on the materials used, phase-correcting structures can be dielectric[28], metallic[29], or printed patch[30]. Only dielectric PCMs are bulky and suffer from ionization problems in higher frequency operation[31]. In contrast, only metallic PCMs consist of multiple metal layers separated by an air gap to provide sufficient phase coverage[32–34]. Printed patch-based PCMs also use multiple printed slabs bonded with prepregs materials, offering a compact solution for phase correction.

Only dielectric phase-correcting surfaces reported in the literature[35,36] for NFPT were traditionally machined from a thick block of commercial-off-the-shelf (COTS) dielectric materials with CNC machines[37]. In this process, there is a high possibility of breakdown and cracking of the structure due to fragile materials like ceramic when the machine switches to different sizes of drill bits to create slots of varying dimensions. The latest advancements in 3-D printing technology and materials have been a blessing in mitigating the difficulties significantly associated with conventional manufacturing methods to fabricate tiny and complex structures[38].

Several 3-D printed dielectric phase-transforming structures have been reported in the literature, utilizing traditional 3-D printing materials such as ABS[7,39,40] and PLA. While these materials are cost-effective, their permittivity is limited to a range of 2.5 to 3, and they suffer from high RF loss, making them inefficient for high-frequency communication due to high RF loss and bulky size. Some recently developed 3-D printing materials have low RF loss compared to traditional 3-D printed materials that can be used to fabricate the PCMs, which provides better performance. For instance, PREPERM®ABS materials offer different permittivity options and exhibit low RF loss compared to traditional 3-D design materials like PLA or ABS, thereby providing better RF performance across a wide range of frequencies. Several 3-D printed phase-correcting structures have been reported in the literature to improve the performance of aperture-type antennas. Some of them are non-planar, and others are planar but with high profile[7].

Our main contribution in this paper is the design of a low-profile metastructure for near-field phase correction of aperture-type antennas, offering a significant improvement over state-of-the-art phase-correcting structures. To reduce the height of the metastructure, we propose a novel approach to designing 3-D printable, highly transmitting ($S21 > -1dB$) meta-atoms, also known as unit cells, using composite metal and dielectric materials. The meta-atoms used in the proposed phase-transforming metastructure are metalized and different from printed patch unit cells used in the previous studies[37,41]. In the patch unit cells, prepregs are used to print the metallic patch on a substrate. Our metalized cell design avoids the use of prepregs, presenting a novel approach that, to our knowledge, has not been previously proposed. The height of our proposed PCM is 6.25 mm ($0.25\lambda$), making it lower than previously published all-dielectric or all-metal structures. Additionally, unlike non-planar phase-correcting structures, our proposed planar PCM does not suffer from losses due to the shadowing effect. Along with its planar and low-profile characteristics, the proposed metastructure is also polarization-independent.

## Design methodology of the proposed PCM

A cross-sectional view of a classical resonant cavity antenna (RCA) with a phase-correcting metastructure is shown in Fig. 1a to describe the methodology of the proposed PCM design using the near-field phase transformation approach. Though the proposed phase-correcting metastructure can be scaled to any type of aperture antenna, an RCA is considered here as an example to compare the results of the proposed system with existing phase-correcting structures for RCA reported in the literature. The design frequency for the prototype of the proposed PCM is set at 12 GHz. The RCA consists of a copper ground plane and a partially reflecting surface

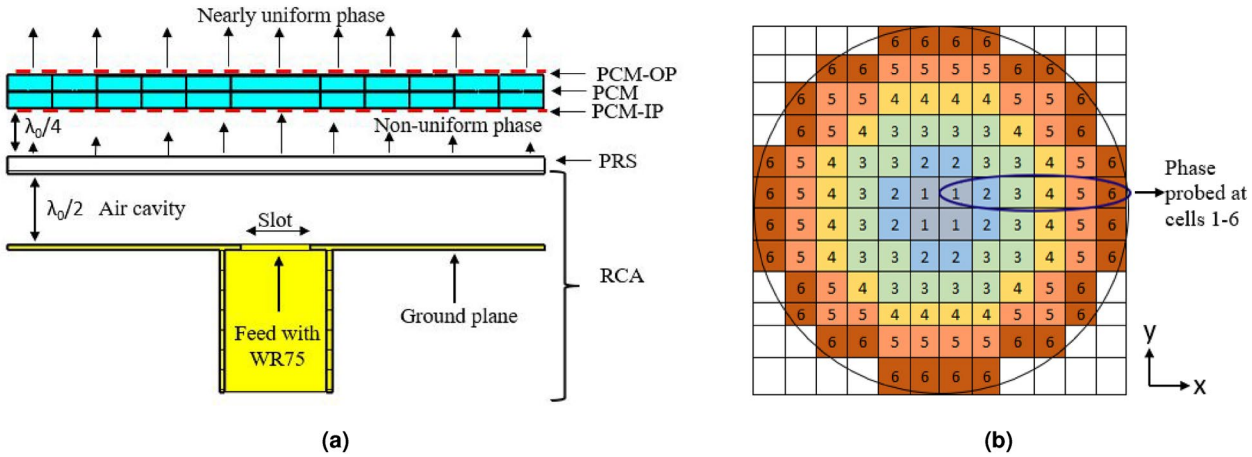


**Figure 1.** (**a**) Cross-sectional view of a classical RCA with the proposed PCM. (**b**) Circularly symmetric unit cell distribution followed for phase correction above antenna aperture.

(PRS) of dimensions $100mm \times 100mm$ ($4\lambda_0 \times 4\lambda_0$) placed at a distance of $\lambda_0/2$ from the ground plane, where $\lambda_0$ is the free space wavelength at 12 GHz. The PRS is made from Rogers TMM4 material, which has a permittivity ($\epsilon_r$) of 4.7 and loss tangent ($\tan\delta$) of 0.002. The thickness of the ground plane and PRS are 1 mm and 3.175 mm, respectively. The distance between the ground plane and PRS is chosen as 13 mm ($\approx \lambda_0/2$) to fulfill the requirement of resonance condition between ground and PRS[36]. The PCM is placed at a distance of 7 mm ($\approx \lambda_0/4$) from the PRS to shift the maximum directivity to or near to the design frequency.

The RCA is excited by a slot antenna with slot dimensions of $13.05mm \times 8.53mm$ using a commercially available WR-75 waveguide. Resonance occurs in the air cavity between the ground plane and PRS at 12.4 GHz due to the back and forth of the EM wave generated from the source. The electric field ($E_y$) phase distribution on the antenna aperture is not uniform, as indicated with unequal arrows in Fig. 1a, which causes poor far-field radiation performance. To address this, a phase-transforming structure is placed at a distance of $\lambda_0/4$ to transform the non-uniform phase into a more uniform phase. In Fig. 1a, the phases on the input surface plane (PCM-IP) are non-uniform, whereas the phases on the output surface plane (PCM-OP) are nearly uniform due to the phase correction provided by phase-correcting metastructure (PCM).

The metastructure is designed using the near-field phase-correction technique following the approach described in Ref.[37]. First, an imaginary plane, denoted by PCM-IP, is considered above the antenna aperture at a distance of $\lambda_0/4$ to probe the actual phase of the dominant electric field ($E_y$). This virtual plane is divided into a 2-D grid of $12 \times 12$ squares, with each cell having a size of 8.33 mm ($\lambda_0/3$), as shown in Fig. 1b. Detailed explanations of selecting the cell size and the square grid are provided in Ref.[42]. The phase of the dominant electric field is probed at the center of each square in the grid. A reference phase is then set up to correct the probed phases to this reference phase.

The required phase delays for phase correction relative to the reference phase in each square grid are generated by placing appropriate meta-atoms on the individual square grids. The required ideal phases for all meta-atoms are calculated by using the following equation:

$$\theta_r(x, y) = \theta_o - \theta_i \tag{1}$$

where $\theta_i$ represents the phases on the PCM-IP plane, $\theta_o$ represents the phases on the PCM-OP plane shown in Fig. 1a and the required ideal phase delay is denoted by $\theta_r(x, y)$.

Since the phase distribution on top of the antenna aperture is considered circularly symmetric around its center, the phases are probed at the center of only cells 1 to 6 along the x-axis, shown in Fig. 1b. The distance from the origin to the centers of these six cells, along with their corresponding probed phases, are listed in Table 1. The reference phase is set to $\theta_o$=200° for phase correction, and the required phase delays are calculated accordingly. For example, the distance between the origin (0,0) and the center of cell 3 is 20.825 mm, and the probed phase at that position is 49.37°. To correct this phase to 200°, a phase delay of 150.63° (=200–49.37) is needed at the location of cell 3. All other phases are calculated similarly. The meta-atoms are selected in such a way that they can produce the required phase delay for each location of the six cells. These meta-atoms are then repeated and organized in a concentric circular and symmetric pattern, as shown in Fig. 1b, to form the complete phase-correcting metastructure.

## Proposed 3-D printed meta-atoms and PCM design

The widely used approach to designing and investigating metastructure begins with the design and analysis of meta-atoms, which are the basic building blocks used to control the RF response of the metastructure. Initially, the performance of the meta-atoms, also called unit cells, is analyzed. Based on this analysis, appropriate meta-atoms are then assembled to form the desired phase-correcting metastructure.

### Meta-atoms analysis

In our proposed 3D printed PCM, three types of highly electromagnetic signal-transmitting single-layer meta-atoms are used, as shown in Fig. 2. We used hybrid cells because a single cell is not capable of generating a wide range of phases with low height while maintaining a transmission coefficient greater than – 1 dB. All the meta-atoms are cuboid with a height of 6.25 mm ($\lambda_0/4$). According to the definition of metasurface, the lateral dimensions of the meta-atoms, also known as unit cells, should be the sub-wavelength of the propagating wave. From the meta-atom analysis reported in Refs.[23,32,43,44], it appears that the meta-atom size can be as large as $\lambda_0/3$ without negatively affecting the accuracy of the results. Therefore, the lateral dimensions of the proposed meta-atom are selected as 8.33 mm ($\lambda_0/3$)[37], where $\lambda_0$ (=25 mm) is the operating wavelength of the electromagnetic

| Cell number | Center position of the cells (mm) | Probed phases (°) | Required phase delay (°) | Values of 'b' (mm) |
|---|---|---|---|---|
| 1 | 4.165 | 118.3 | 81.7 | 3.71 |
| 2 | 12.495 | 90.47 | 109.53 | 3.87 |
| 3 | 20.825 | 49.37 | 150.63 | 3.5 |
| 4 | 29.155 | 9.12 | 190.88 | 3.36 |
| 5 | 37.485 | – 30.65 | 230.65 | 4.82 |
| 6 | 45.815 | – 50.59 | 250.59 | 5.6 |

**Table 1.** Cells center positions, probed phases, required phase delay, and values of 'b' for the meta-atoms.

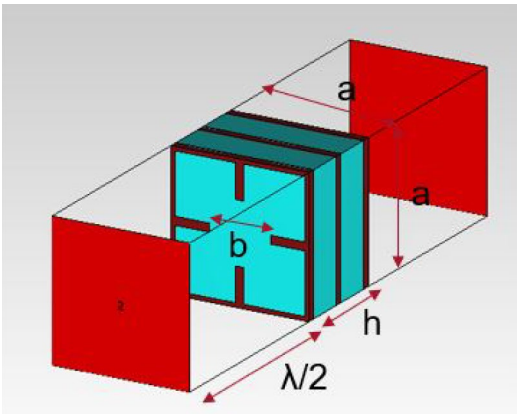


**(a)** Meta-atom type-I (MA-1, MA-2).

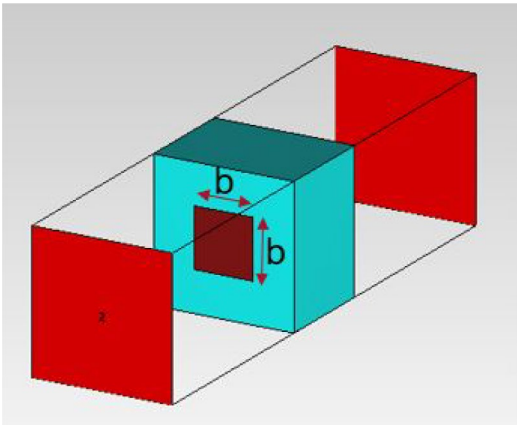


**(b)** Meta-atom type-II (MA-3).

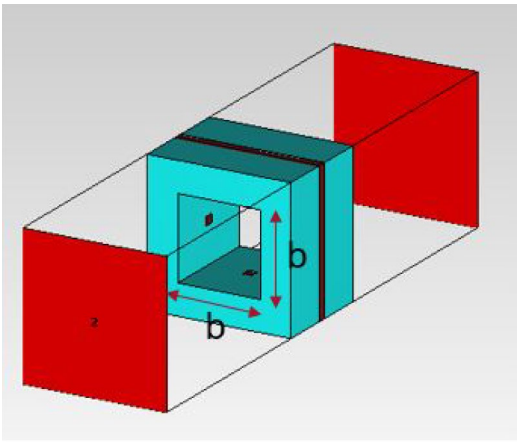


**(c)** Meta-atom type-III (MA-4, MA-5, MA-6).

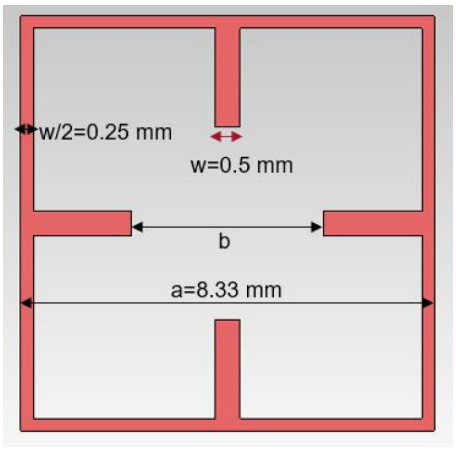


**(d)** Metal layer dimensions (for Meta-atoms type-I and III).

**Figure 2.** Three types of meta-atom in a simulation environment and metal layer dimensions.

wave in the design frequency (12 GHz). This relatively large meta-atom size ($\lambda_0/3$) also reduces the design and fabrication complexity. The cuboid structure is made of dielectric material with a dielectric constant ($\epsilon_r$) of 4.5 and loss tangent ($\tan\delta$) of 0.0042 and copper.

The meta-atoms (MA) used in the inner two concentric circular layers (MA-1, MA-2) of the proposed 3-D printable, planar PCM are similar and denoted as meta-atom (MA) type-I, depicted in Fig. 2a. In meta-atom type-I, three identical metal layers are inserted at equal vertical distance on the cube's top, bottom, and middle. The metal layers are cross-shaped with a central cut (cutting length is denoted by b). The metal layer has a thickness of 0.5 mm. The width of the outer metal boundary is 0.25 mm, and the width of the inner metal arms is 0.5 mm, as shown in Fig. 2d. By varying the length of the inner metal arms, the phase generated by the meta-atom can be changed as the permittivity changes. The meta-atoms used in the subsequent circular pattern (MA-3) are denoted as type-II, shown in Fig. 2b, where a metal block is inserted in the middle of the substrate. The lateral dimension of this metal block (b) is equal to 3.36 mm, and the height is equal to the meta-atom height (6.25 mm).

The meta-atoms used in the outer three concentric circular rings (MA-4, MA-5, MA-6) in the proposed 3-D printed PCM are similar and denoted as meta-atom type-III, shown in Fig. 2c. Each meta-atom type-III consists of a single metal layer inserted in the middle of the substrate, with the same thickness and width as the metal layer used in meta-atom type-I. The dimension of the central air hole (denoted as b) varies to generate different required phases.

The proposed meta-atoms are designed, and full-wave simulation is done from 11 GHz to 15 GHz using Computer Simulation Technology (CST) Microwave Studio software. Excitation is given by a waveguide port, and periodic boundary conditions were set in the simulation environment to simulate the proposed meta-atoms. To predict the transmission and reflection characteristics of the proposed meta-atoms using full-wave simulations, for each type of meta-atom, the value of 'b' is varied with a parametric sweep with a step size of 0.02 and a database of transmission magnitude and phase for each type of meta-atom is created. From the database, the meta-atoms with transmission magnitudes greater than -1 dB are filtered and separated to design the proposed highly transmitting metastructure.

The required phase delays at the centers of the selected six cells, derived from electric field aperture phase distribution, are 81.7°, 109.53°, 150.63°, 190.88°, 230.65°, and 250.59°, and the values of 'b' for the selected

meta-atoms 1 to 6 to provide the phase delays in mm are 3.71, 3.87, 3.5, 3.36, 4.82 and 5.6, respectively, mentioned in Table 1. The magnitude and phase of the transmission coefficients of the six meta-atoms used in the proposed PCM are shown in Fig. 3. From the transmission characteristic curves, it is noted that the transmission coefficient magnitudes of the cells are greater than − 0.72 dB at 12 GHz. Due to the high transmission characteristics of the individual cell, the proposed metastructure is also highly RF signal-transmissive and provides enhanced gain and directivity with low RF loss.

## Proposed phase-correcting metastructure

As the electric field phase distribution on top of the RCA aperture is considered circularly symmetric as shown in Fig. 1b, for design simplicity, only the six meta-atoms are repeated and organized in a concentric circularly symmetric pattern to form the proposed highly transmitting planar phase-correcting metastructure. A perspective view of the proposed 3-D printable PCM is shown in Fig. 4. The cells located at the corner of the PCM are ignored for simplicity in design and reduced weight, as those cells have minimal impact on the overall performance.

## Result analysis

After completing the design of the whole system, including the RCA and the proposed phase-correcting metastructure, the system is simulated with a time domain solver of commercially available Computer Simulation Technology (CST) microwave studio software (v.2022) over a frequency range of 11–14 GHz.

The normalized phase distribution of the dominant electric field ($E_y$) on top of the antenna aperture along the x-axis at a distance of 6.25 mm ($\lambda/4$), both with and without the PCM, is shown in Fig. 5a. This figure indicates the degree of nonuniformity in the aperture phase distribution of the base antenna. For the RCA without PCM, the phase difference between the maximum and minimum phase, known as phase error, is 176°. With the proposed PCM, the phase error is reduced to 82°, demonstrating the improved phase uniformity in aperture phase distribution. This enhancement in phase uniformity significantly improved the far-field radiation performance. Fig. 5b and c illustrate the 2-D $E_y$ phase distribution on top of the antenna aperture looking from the z-axis at a distance of 6.25 mm, without and with the proposed PCM, respectively. The former clearly shows the highly non-uniform phase distribution of the base antenna without PCM, while the latter displays the more uniform phase distribution achieved with the proposed PCM.

Figure 6 shows the variation in peak directivity and gain across different frequencies in the E-plane, both with and without the proposed phase-correcting metastructure. While the RCA without PCM provides its maximum performance (peak directivity of 12.3 dB and gain of 12.2 dB) at 12 GHz, maximum performance is achieved for RCA with the proposed PCM at 12.4 GHz due to the loading of PCM on top of the aperture. The peak directivity and gain of the RCA with the proposed PCM at 12.4 GHz are 20 dB and 19.5 dB, respectively. The small shifting of frequency of peak directivity is due to the loading of the proposed PCM, and it is a common phenomenon in the case of near-field phase correction. This figure also indicates a 3-dB directivity bandwidth of 16.50% of the antenna with the proposed PCM.

The improvement in far-field radiation performance using the proposed PCM is demonstrated in Fig. 7. The directivity and gain patterns in the E-plane and H-plane at 12.4 GHz are shown in Fig. 7a and b, respectively. With the proposed PCM, the RCA achieves a peak directivity of 20 dBi, compared to 11.4 dBi without the PCM. At 12.4

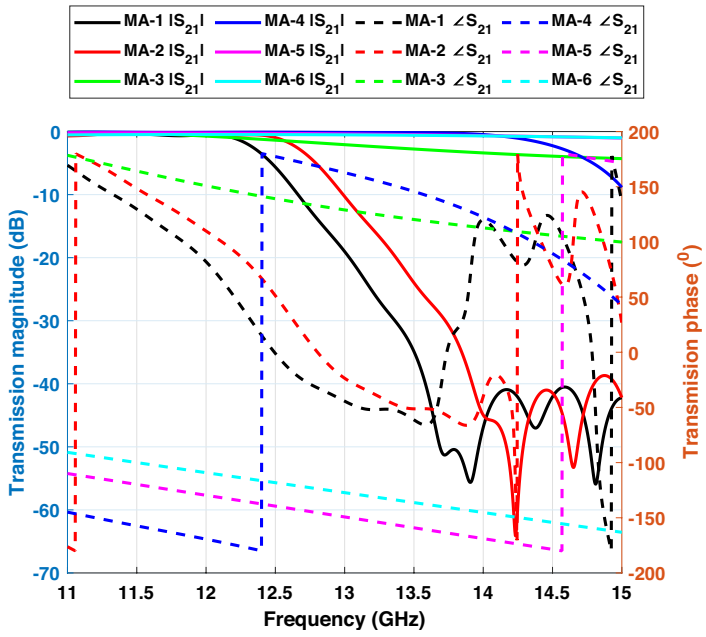


**Figure 3.** Transmission magnitude and phase of the meta-atoms (MA) used in the proposed PCM.

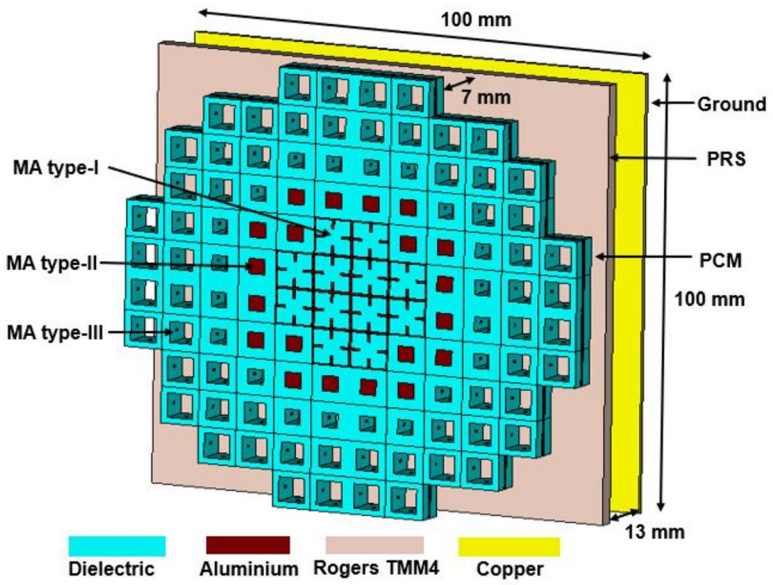


**Figure 4.** Perspective view of the proposed PCM along with RCA.

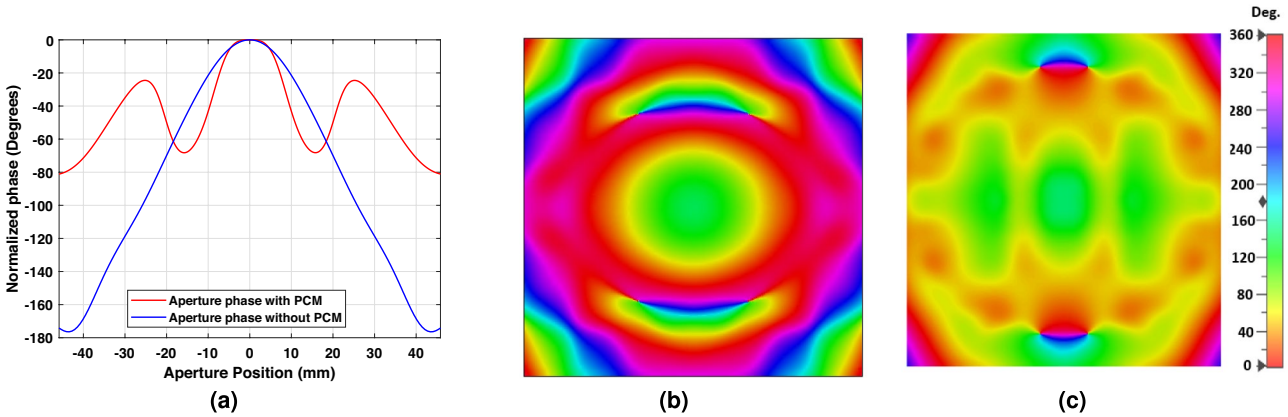


**Figure 5.** (**a**) Normalized E-field ($E_y$) phase distribution above aperture at a distance of 6.25 mm with and without PCM. (**b**) 2-D phase distribution on top of the aperture without PCM. (**c**) 2-D phase distribution on top of the aperture with PCM.

GHz, the peak gains for the RCA with and without PCM are 19.5 dB and 11.2 dB, respectively. This indicates an improvement of 8.6 dB in directivity and 8.3 dB in gain, attributed to the enhanced near-field phase distribution provided by the proposed PCM. Additionally, the side-lobe levels (SLLs) of the RCA without PCM are -7.3 dB in the E-plane and – 20.8 dB in the H-plane. With the PCM, the SLLs improve to – 10 dB in the E-plane and – 23.1 dB in the H-plane. This enhancement in antenna performance is due to the improved phase uniformity on the antenna aperture phase distribution. The peak aperture efficiency of the RCA with the proposed PCM is 41.46%.

To verify the results obtained from CST software, we conducted simulations of our prototype using another commercial electromagnetic 3D full-wave simulator, HFSS (High-frequency Structure Simulator). The results from both software shows good agreement. Comparative results from both simulators are presented in Figs. 8, 9 and 10.

Figures 8 and 9 depict the radiation patterns at 11.6, 12, 12.4, and 12.8 GHz in the E-and H-plane, respectively, utilizing both CST and HFSS software. Both co-polar and cross-polar components are shown for each plane. The peak gain at 11.6, 12, 12.4, and 12.8 GHz using CST are 16.9, 19, 19.5, and 18.7 dB, respectively. The proposed antenna system exhibits impressive cross-polar rejection in the peak beam direction, with cross-polar components being at least 35 dB lower than the co-polar components across all frequencies in both principal planes. From Figs. 8 and 9, it is observed that the co-polar component patterns from both software show good agreement. Although there is a small difference in cross-polar component patterns between CST and HFSS, the level of cross-polar rejection remains similar in both software. This discrepancy in cross-polar components can be attributed to the computational accuracy of each software.

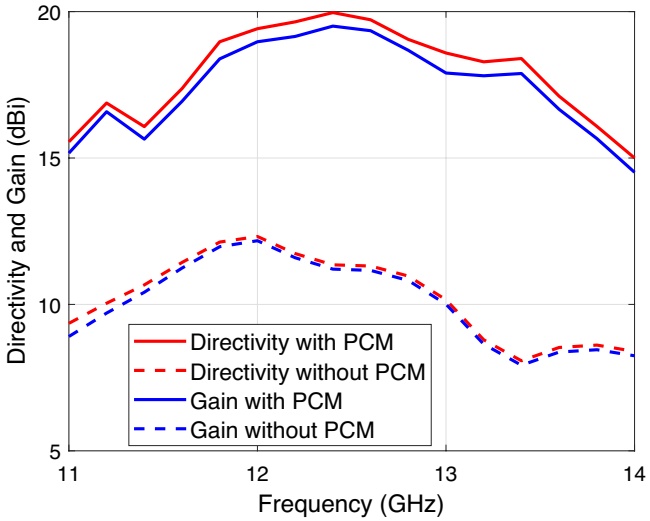


**Figure 6.** Directivity and gain variation within the operational bandwidth.

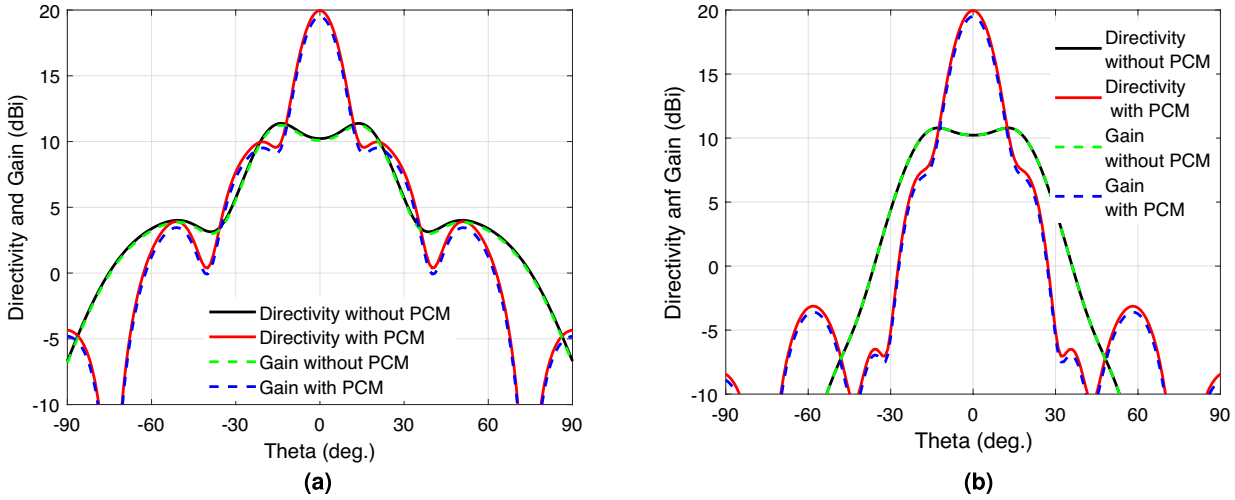


**Figure 7.** Radiation pattern comparison between RCA with and without PCM at 12.4 GHz in (**a**) E-plane (**b**) H-plane.

The reflection coefficients ($S_{11}$) of the resonant cavity antenna with the PCM, simulated using both CST and HFSS software, are shown in Fig. 10. From this figure, it is clearly observed that $S_{11}$ is less than -13 dB, indicating that more than 90% of power is transmitted through the proposed PCM system. Additionally, the voltage standing wave ratio (VSWR) of the RCA is also presented in this figure with PCM for both CST and HFSS simulations. The antenna is well impedance matched over the frequency range of 11 GHz to 14 GHz as the VSWR is below 1.6, as shown in Fig. 10. A good agreement exists between the results obtained from both software packages.

The performance of our proposed phase-correcting metastructure is compared with some state-of-the-art literature for benchmarking shown in Table 2. In this comparison table, the thickness of the proposed PCM is only 6.25 mm (0.25 $\lambda$), which is the lowest among all the structures. Furthermore, the RCA with our proposed PCM achieves a peak directivity of 20 dBi and a 3-dB directivity bandwidth (BW) of 16.50%, which are comparable with other designs. The reduced height of our proposed PCM leads to lower material consumption during manufacturing, resulting in cost savings when produced with a multi-material 3-D printer.

Commercial-off-the-shelf (COTS) 3D printing material, such as PREPERM material with a dielectric constant of 4.5 and loss tangent of 0.0042, along with copper, can be utilized to fabricate meta-atoms using multi-material 3-D printers. The permittivity and loss characterization of similar dielectric material, like PREMIX PREPERM TP20280, are detailed in Refs.[48–50], demonstrating their suitability for achieving desired performance. As recent advancements in additive manufacturing (AM) technology have led to the emergence of novel 3-D printing methods and materials, some new generation 3-D printers are capable of fabricating conductive and dielectric materials simultaneously[51]. For instance, authors in Refs.[52–54] successfully fabricated some prototypes integrating metal and dielectric material using the additively manufactured electronics (AME) method and DragonFly$^{TM}$ 3D printer, achieving desired performance through experimental validation. Thus, similar techniques can feasibly

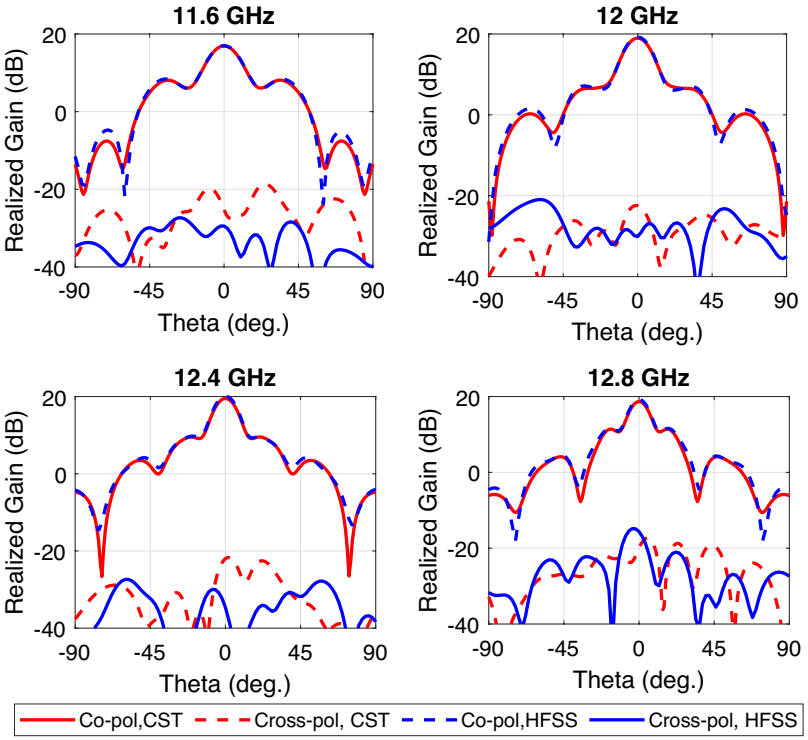


**Figure 8.** Comparison of far-field pattern in E-plane at 11.6, 12, 12.4, and 12.8 GHz, obtained from CST and HFSS.

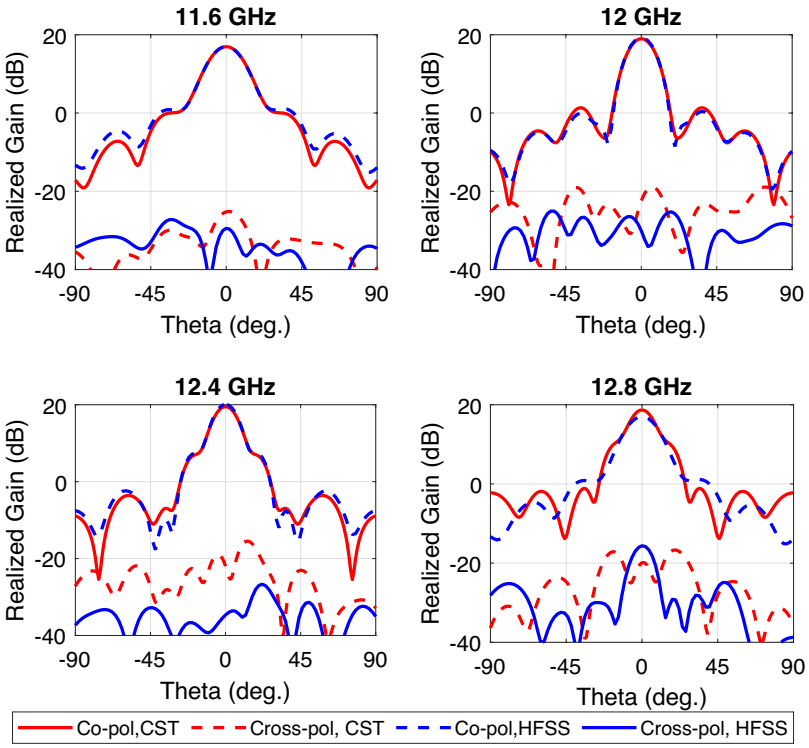


**Figure 9.** Comparison of far-field pattern in H-plane at 11.6, 12, 12.4, and 12.8 GHz, obtained from CST and HFSS.

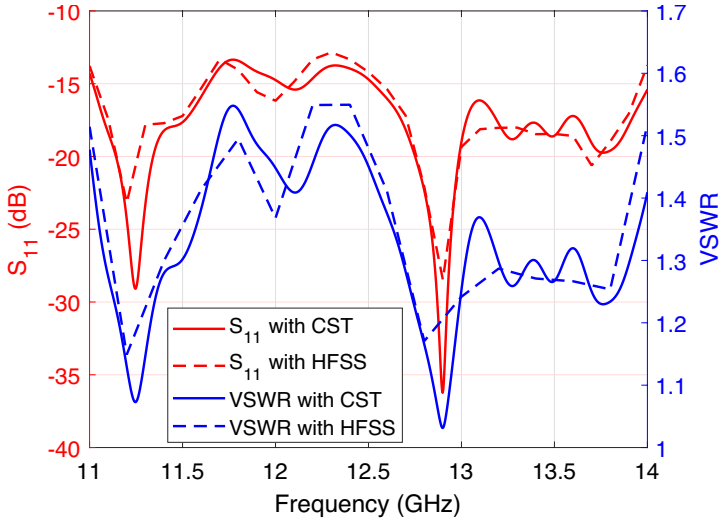


**Figure 10.** Comparison of reflection coefficient and VSWR results between CST and HFSS simulations.

| References | Peak directivity (dB) | SLLs (dB) | 3-dB directivity BW (%) | PCM height (mm) | Cost |
|---|---|---|---|---|---|
| This paper | 20 | − 10 | 16.50% | 6.25 (0.25$\lambda$) | Low |
| Reference[7] IEEE access | 21.12 | − 17.2 | n/a | 25 (0.92 $\lambda$) | Low |
| Reference[38] IEEE AWPL | 20.3 | − 17 | 9.40% | 21 (0.77 $\lambda$) | Low |
| Reference[45] IEEE AWPL | 22 | − 14.3 | 10% | 21.7 (0.81$\lambda$) | High |
| Reference[46] IEEE TAP | 21.1 | − 11 | 41% | 34 (1.25$\lambda$) | High |
| Reference[47] IEEE AWPL | 16.05 | − 10.4 | 49.65% | 13.5 (0.5$\lambda$) | Low |

**Table 2.** Comparison of the proposed PCM with other state-of-the-art structures in literature. *IEEE AWPL* - IEEE antennas and wireless propagation letters, *IEEE TAP* - IEEE transactions on antennas and propagation.

be employed to fabricate our proposed prototype, which incorporates both metal and dielectric components. Alternatively, conventional 3D printers can be used to fabricate our proposed prototype. In this approach, the dielectric component needs to be printed in two parts with a conventional printer. The metal parts can be produced from a metal sheet using a laser cutter. Subsequently, the metal and dielectric components can be assembled together to construct the entire metasurface.

## Conclusion

A new approach to designing 3-D printed hybridized meta-atoms is presented for low-profile phase-correcting hybrid metastructure development using metal and dielectric materials for aperture-type antenna performance enhancement. Our proposed PCM is planar, highly transparent, and can be fabricated in a single step at a low cost using modern additive manufacturing techniques. Additive manufacturing evades the challenges associated with fabricating intricate and delicate structures using traditional manufacturing processes. The low profile of the proposed PCM makes it cost-effective with 3-D printing technology. To our knowledge, its profile is lower than that of structures previously reported in the literature, making it suitable for compact antenna systems requiring high performance. The proposed system with waveguide feed RCA achieves excellent performance with peak directivity and gain of 20 dBi and 19.5 dB, respectively, at 12.4 GHz. Moreover, it exhibits a lower side lobe level (-10 dB) and high aperture efficiency of 41.46%. Commercially available PREPERM®ABS dielectric material with low RF loss can be used to fabricate the proposed PCM.

## Data availability

All data generated or analyzed during this study are included in this published article. For any further data, you can contact the corresponding author, Md Yeakub Ali (mdyeakub.ali@students.mq.edu.au).

Received: 12 January 2024; Accepted: 25 July 2024
Published online: 02 August 2024

## References

1. Beier, G., Niehoff, S. & Hoffmann, M. Industry 4.0: A step towards achieving the SDGs? a critical literature review. *Discov. Sustain.* **2**, 22 (2021).

2. Godina, R. *et al.* Impact assessment of additive manufacturing on sustainable business models in industry 4.0 context. *Sustainability* **12**, 7066 (2020).
3. Delic, M. & Eyers, D. R. The effect of additive manufacturing adoption on supply chain flexibility and performance: An empirical analysis from the automotive industry. *Int. J. Prod. Econ.* **228**, 107689 (2020).
4. Fasel, U. *et al.* Composite additive manufacturing of morphing aerospace structures. *Manuf. Lett.* **23**, 85–88 (2020).
5. Busachi, A. *et al.* A review of additive manufacturing technology and cost estimation techniques for the defence sector. *CIRP J. Manuf. Sci. Technol.* **19**, 117–128 (2017).
6. Capel, A. J., Rimington, R. P., Lewis, M. P. & Christie, S. D. 3D printing for chemical, pharmaceutical and biological applications. *Nat. Rev. Chem.* **2**, 422–436 (2018).
7. Hayat, T., Afzal, M. U., Lalbakhsh, A. & Esselle, K. P. Additively manufactured perforated superstrate to improve directive radiation characteristics of electromagnetic source. *IEEE Access* **7**, 153445–153452 (2019).
8. Ahmed, F. *et al.* 3D printable synthetic metasurface to realize 2D beam-steering antenna. *IEEE Open J. Antennas Propag.* **4**, 506–519 (2023).
9. Afzal, M. U., Lalbakhsh, A. & Esselle, K. P. Method to enhance directional propagation of circularly polarized antennas by making near-electric field phase more uniform. *IEEE Trans. Antennas Propag.* **69**, 4447–4456 (2021).
10. Ali, A., Kourogiorgas, C., Yates, J., Brown, T. & Khalily, M. Multi-beam reflectarray for future high throughput satellites. In *2023 IEEE International Symposium on Antennas and Propagation and USNC-URSI Radio Science Meeting (USNC-URSI)*, 1139–1140 (IEEE, 2023).
11. Chang, Y.-C. A compact EHF/SHF dual-band reflector antenna. In *Digest on Antennas and Propagation Society International Symposium*, 1602–1605 (IEEE, 1989).
12. Scattone, F., Ettorre, M., Sauleau, R. & Fonseca, N. Leaky-wave-based dual-band phased array for satellite communications. In *2016 10th European Conference on Antennas and Propagation (EuCAP)*, 1–4 (IEEE, 2016).
13. Mao, C.-X., Gao, S., Wang, Y., Chu, Q.-X. & Yang, X.-X. Dual-band circularly polarized shared-aperture array for *c*-/*x*-band satellite communications. *IEEE Trans. Antennas Propag.* **65**, 5171–5178 (2017).
14. Yang, J., Xin, H. & Tang, M.-C. Broadband, low-profile, planar reflectarray antenna based on an achromatic metasurface. *IEEE Trans. Antennas Propag.* **71**, 5440–5445 (2023).
15. Wu, G.-B., Qu, S.-W. & Yang, S. Wide-angle beam-scanning reflectarray with mechanical steering. *IEEE Trans. Antennas Propag.* **66**, 172–181 (2017).
16. Ali, A., Khalily, M. & Tafazolli, R. Ultra-wideband dielectric reflectarray antenna with oam beams for mm-wave applications. In *2022 International Symposium on Antennas and Propagation (ISAP)*, 381–382 (IEEE, 2022).
17. Farias, R. L., Peixeiro, C. & Heckler, M. V. Single-layer dual-band dual-circularly polarized reflectarray for space communication. *IEEE Trans. Antennas Propag.* **70**, 5989–5994 (2022).
18. Vilenskiy, A. R., Makurin, M. N., Lee, C. & Ivashina, M. V. Reconfigurable transmitarray with near-field coupling to gap waveguide array antenna for efficient 2-D beam steering. *IEEE Trans. Antennas Propag.* **68**, 7854–7865 (2020).
19. Su, D. *et al.* A double-layer metal-only huygens' metasurface transmitarray. *IEEE Antennas Wirel. Propag. Lett.* **22**, 1897–1901 (2023).
20. Pham, T. K., Guang, L., González-Ovejero, D. & Sauleau, R. Dual-band transmitarray with low scan loss for satcom applications. *IEEE Trans. Antennas Propag.* **69**, 1775–1780 (2020).
21. Khan, S. *et al.* Miniaturization of dielectric resonator antenna by using artificial magnetic conductor surface. *IEEE Access* **8**, 68548–68558 (2020).
22. Abedian, M. *et al.* High isolation circularly polarized in-band full-duplex anisotropic dielectric resonator antenna. *Sci. Rep.* **13**, 5937 (2023).
23. Lalbakhsh, A., Afzal, M. U. & Esselle, K. P. Multiobjective particle swarm optimization to design a time-delay equalizer metasurface for an electromagnetic band-gap resonator antenna. *IEEE Antennas Wirel. Propag. Lett.* **16**, 912–915 (2016).
24. Ponti, C., Baccarelli, P., Ceccuzzi, S., Tognolatti, L. & Schettini, G. Resonant-cavity antennas with tapered and wideband EBG superstrates. In *2021 International Conference on Electromagnetics in Advanced Applications (ICEAA)*, 301–304 (IEEE, 2021).
25. Zhou, L., Duan, X., Luo, Z., Zhou, Y. & Chen, X. High directivity fabry-pérot antenna with a nonuniform partially reflective surface and a phase correcting structure. *IEEE Trans. Antennas Propag.* **68**, 7601–7606 (2020).
26. Khalily, M., Yurduseven, O., Cui, T. J., Hao, Y. & Eleftheriades, G. V. Engineered electromagnetic metasurfaces in wireless communications: Applications, research frontiers and future directions. *IEEE Commun. Mag.* **60**, 88–94 (2022).
27. Church, P., Matheson, J., Cao, X. & Roy, G. Evaluation of a steerable 3D laser scanner using a double Risley prism pair. In *Degraded Environments: Sensing, Processing, and Display 2017* Vol. 10197 (eds Church, P. *et al.*) 203–211 (SPIE, 2017).
28. Hashmi, R. M., Zeb, B. A. & Esselle, K. P. Wideband high-gain EBG resonator antennas with small footprints and all-dielectric superstructures. *IEEE Trans. Antennas Propag.* **62**, 2970–2977 (2014).
29. Ahmed, F., Afzal, M. U., Hayat, T., Esselle, K. P. & Thalakotuna, D. N. A dielectric free near field phase transforming structure for wideband gain enhancement of antennas. *Sci. Rep.* **11**, 14613 (2021).
30. Zhou, L., Chen, X., Duan, X. & Li, J. FPA using a three-layer PSS for gain enhancement. *IET Microw. Antennas Propag.* **12**, 400–405 (2018).
31. Baba, A. A., Hashmi, R. M., Attygalle, M., Esselle, K. P. & Borg, D. Ultrawideband beam steering at mm-wave frequency with planar dielectric phase transformers. *IEEE Trans. Antennas Propag.* **70**, 1719–1728 (2021).
32. Lalbakhsh, A., Afzal, M. U., Esselle, K. P. & Smith, S. L. Low-cost nonuniform metallic lattice for rectifying aperture near-field of electromagnetic bandgap resonator antennas. *IEEE Trans. Antennas Propag.* **68**, 3328–3335 (2020).
33. Zhao, X. *et al.* All-metal beam steering lens antenna for high power microwave applications. *IEEE Trans. Antennas Propag.* **65**, 7340–7344 (2017).
34. Ahmed, F., Afzal, M. U., Hayat, T., Esselle, K. P. & Thalakotuna, D. N. A near-field meta-steering antenna system with fully metallic metasurfaces. *IEEE Trans. Antennas Propag.* **70**, 10062–10075 (2022).
35. Mateo-Segura, C., Dyke, A., Dyke, H., Haq, S. & Hao, Y. Flat luneburg lens via transformation optics for directive antenna applications. *IEEE Trans. Antennas Propag.* **62**, 1945–1953 (2014).
36. Afzal, M. U., Esselle, K. P. & Zeb, B. A. Dielectric phase-correcting structures for electromagnetic band gap resonator antennas. *IEEE Trans. Antennas Propag.* **63**, 3390–3399 (2015).
37. Afzal, M. U. & Esselle, K. P. A low-profile printed planar phase correcting surface to improve directive radiation characteristics of electromagnetic band gap resonator antennas. *IEEE Trans. Antennas Propag.* **64**, 276–280 (2015).
38. Hayat, T., Afzal, M. U., Lalbakhsh, A. & Esselle, K. P. 3-D-printed phase-rectifying transparent superstrate for resonant-cavity antenna. *IEEE Antennas Wirel. Propag. Lett.* **18**, 1400–1404 (2019).
39. Hayat, T. *et al.* The use of a pair of 3D-printed near field superstructures to steer an antenna beam in elevation and azimuth. *IEEE Access* **9**, 153995–154010 (2021).
40. Pepino, V. M., da Mota, A. F., Martins, A. & Borges, B.-H.V. 3-D-printed dielectric metasurfaces for antenna gain improvement in the ka-band. *IEEE Antennas Wirel. Propag. Lett.* **17**, 2133–2136 (2018).
41. Singh, K., Afzal, M. U., Kovaleva, M. & Esselle, K. P. Controlling the most significant grating lobes in two-dimensional beam-steering systems with phase-gradient metasurfaces. *IEEE Trans. Antennas Propag.* **68**, 1389–1401 (2019).

42. Lalbakhsh, A., Afzal, M. U., Esselle, K. P. & Zeb, B. A. Multi-objective particle swarm optimization for the realization of a low profile bandpass frequency selective surface. In *2015 International Symposium on Antennas and Propagation (ISAP)*, 1–4 (IEEE, 2015).
43. Xie, P., Wang, G., Li, H. & Gao, X. A novel methodology for gain enhancement of the fabry-pérot antenna. *IEEE Access* **7**, 176170–176176 (2019).
44. Singh, K., Afzal, M. U. & Esselle, K. P. Accurate optimization technique for phase-gradient metasurfaces used in compact near-field meta-steering systems. *Sci. Rep.* **12**, 4118 (2022).
45. Afzal, M. U., Esselle, K. P. & Lalbakhsh, A. A methodology to design a low-profile composite-dielectric phase-correcting structure. *IEEE Antennas Wirel. Propag. Lett.* **17**, 1223–1227 (2018).
46. Lalbakhsh, A., Afzal, M. U., Esselle, K. P. & Smith, S. L. Wideband near-field correction of a fabry-pérot resonator antenna. *IEEE Trans. Antennas Propag.* **67**, 1975–1980 (2019).
47. Hayat, T. *et al.* Low-cost ultrawideband high-gain compact resonant cavity antenna. *IEEE Antennas Wirel. Propag. Lett.* **19**, 1271–1275 (2020).
48. Paraskevopoulos, A. *et al.* 3-D printed all-dielectric GRIN lens antenna with an integrated feeder. *IEEE Open J. Antennas Propag.* **4**, 528–536 (2023).
49. Zhang, S. *et al.* Ultra-wideband flat metamaterial GRIN lenses assisted with additive manufacturing technique. *IEEE Trans. Antennas Propag.* **69**, 3788–3799 (2020).
50. Poyanco, J.-M., Pizarro, F. & Rajo-Iglesias, E. Cost-effective wideband dielectric planar lens antenna for millimeter wave applications. *Sci. Rep.* **12**, 4204 (2022).
51. Flowers, P. F., Reyes, C., Ye, S., Kim, M. J. & Wiley, B. J. 3d printing electronic components and circuits with conductive thermoplastic filament. *Addit. Manuf.* **18**, 156–163 (2017).
52. Li, M., Yang, Y., Iacopi, F., Nulman, J. & Chappel-Ram, S. 3D-printed low-profile single-substrate multi-metal layer antennas and array with bandwidth enhancement. *IEEE Access* **8**, 217370–217379 (2020).
53. Zhu, J., Yang, Y., Lai, J. & Nulman, J. Additively manufactured polarization insensitive broadband transmissive metasurfaces for arbitrary polarization conversion and wavefront shaping. *Adv. Opt. Mater.* **10**, 2200928 (2022).
54. Zhu, J. *et al.* Additively manufactured millimeter-wave dual-band single-polarization shared aperture fresnel zone plate metalens antenna. *IEEE Trans. Antennas Propag.* **69**, 6261–6272 (2021).


## Acknowledgements

This work was supported in part by the Icelandic Research Fund Grant 2410297, and by National Science Centre of Poland Grant 2020/37/B/ST7/01448, and in part by the Macquarie University International Research Stipend Program (RTP) scholarship funded by the Commonwealth Government (Scholarship Allocation Number: 20225175).

## Author contributions

M.Y. A.- Background study, conceptualization, model design, simulation, data analysis, manuscript writing, and editing; A.L.- Supervision, technical suggestion, manuscript review; S.K.- Results analysis and review of the manuscript; L.G.- Results analysis, review of the manuscript and funding acquisition; F.A.- Simulation, data analysis, and manuscript review; M.A.- Supervision, intellectual suggestion and review of the manuscript.

## Competing interests

The authors declare no competing interests.

## Additional information

**Correspondence** and requests for materials should be addressed to M.Y.A. or A.L.